Canadian Chemical Transactions Year 2015 | Volume 3 | Issue 4 | Page 410-429

Research Article

DOI:10.13179/canchemtrans.2015.03.04.0235

Synthesis of AC-Bi@SiO_2 Nanocomposite Sphere for Superior Photocatalytic Activity Towards the Photodegradation of Malachite Green

V. L. Chandraboss, J. Kamalakkannan and S. Senthilvelan*

Department of Chemistry, Annamalai University, Annamalainagar 608 002, Tamilnadu, India

**Corresponding Author, Email: dr_senthilvel@yahoo.co.in*

Received: *September 21, 2015* ***Revised:*** *November 20, 2015* ***Accepted:*** *November 24, 2015* ***Published:*** *November 25, 2015*

Abstract: Activated charcoal (AC) supported bismuth (Bi) doped SiO_2 nanocomposite sphere was successfully synthesized via a sol-gel method and utilized in aqueous solution for the photocatalytic degradation of malachite green (MG), a common water pollutant in the textile industry. The structural, morphological and photocatalytic properties of as-synthesized samples were studied using various analytical techniques. Surface morphology and bulk composition of the composite was obtained using electron microscopy with energy dispersive X-ray analysis. An HR-SEM and HR-TEM image of AC-Bi@SiO_2 shows that the spherical particles with an average size around 40 nm. The data of HR-TEM and X-ray diffraction prove that the incorporation of Bi^{3+} into the SiO_2 matrix. The crystal structure and elemental composition was analyzed by combining Fourier transform-Raman spectroscopy and X-ray photoelectron spectroscopy. Surface area of the samples as calculated by BET analyzer and it was found to be 9.18 and 16.4 m^2/g for SiO_2 and AC-Bi@SiO_2 respectively. BET analysis confirmed a significant increase in surface area of the synthesized AC-Bi@SiO_2. UV-vis diffuse reflectance spectra of AC-Bi@SiO_2 show that decrease in the band gap energy. The production of hydroxyl radicals on the surface of the UV-irradiated catalysts was detected by a PL technique using coumarin as a probe molecule. Comparing with the catalyst was synthesized via undoped-SiO_2, modified-SiO_2 exhibits higher photocatalytic activity under ultra-violet (365 nm) irradiation. The possible reasons for enhance photocatalytic performance by Bi^{3+} encapsulation and dye adsorption on AC surfaces were proposed. It has been considered that the large specific surface area, increase of $^{\bullet}OH$ radicals, decreasing band gap energy and electron–hole pair recombination have strong influence on the improvement of photocatalytic activity.

Keywords: Photocatalysis, Activated charcoal, Nanocomposite, Malachite green, UV-light.

1. INTRODUCTION

Malachite green (MG) is a kind of triphenylmethane dye. It is a one of the carcinogen organic molecule [1,2], still illegally used in aquaculture as a fungicide on larvae and juvenile fish [3]. MG is a widely used biocide in the aquaculture industries. It is very effective against protozoal and fungal

infections [4,5] and widely used in ceramics, paper, textile, cell coloring and food coloring industries [6-8]. The US Food and Drug Administration has nominated MG as a priority chemical for carcinogenicity testing [9], it is still being used in many parts of the world due to its low cost, availability and efficacy [10]. In earlier reports [11-13], the photodegradation of MG was investigated. Most studies have interested on advanced photocatalysts, the effects of experimental conditions, and the probability of environmental application.

Therefore, there is a need to develop a novel treatment that is more effective in eliminating MG dye from the wastewater. Advanced oxidation processes (AOPs) are alternative techniques for destructing dyes in industrial waste water treatment [14,15]. They were developed to meet the increasing demand of an effective wastewater treatment. Heterogeneous photocatalysis is an increasing technique for environmental remediation, where semiconductor metal oxides are used as photocatalysts. When organic dyes are decomposed by heterogeneous catalytic reactions, the dye containing waste water was adsorbed on the surface of the photocatalysts, where chemical bonds are broken and formed, and finally small organic molecules are released as decomposed products [15,16].

The environmentally significant application of bismuth (Bi) is low toxicity compared to the heavy metals such as Cd, Sn, Hg, In and Pb. Bi-doped materials are promising candidates in environmental remediation [17,18]. The doped Bi an appropriate content can trap the photogenerated carrier, inhibit their recombination, expand the light absorption and improve the photogenerated radicals [19,20]. The above factors are supporting the enhanced photocatalytic activity of Bi-doped materials.

Silica is suitable in many areas such as ceramics, glass industries, photovoltaic cells and it is also used as catalytic support [21,22]. However, SiO_2 exhibits measurable activities for some catalytic and photocatalytic reactions [23-27]. Recently, bi-metal and tri-metal doped SiO_2 has become of interest in promoting photocatalytic reactions under UV- light irradiation [28-30]. Nowadays, the sol-gel technique is the most commonly employed for the synthesis of silica as well as metal doped SiO_2 core-shell matrices can be achieved [30]. This route involves simultaneous hydrolysis and condensation of alkoxides, so that silica with several characteristics can be succeeded [31,32].

Various supported materials have been proposed for degradation of several dye molecules [33-35]. Activated charcoal is excellent adsorbent of countless pollutants. It is very promising for two reasons: (1) AC is able to adsorb the dye molecules and then release them onto the surface of the catalysts. (2) The intermediates produced during degradation can be also adsorbed by AC and then further oxidized [36,37]. Their industrial applications involve the adsorptive removal of odour, colour, taste and other undesirable organics from industrial wastewater [38].

In this work sol-gel route was utilized for synthesis of AC-supported $Bi@SiO_2$ nanocomposite sphere, and the obtained material was employed in photocatalysis. The synthesized samples were characterized by HR-SEM with EDX, XRD, XPS, BET, FT-RAMAN, DRS and PL analysis. The photocatalytic activity of SiO_2 can be improved by the doping of Bi^{3+} and supported by AC, which increases the available surface area of the SiO_2, allowing an increase in adsorption of MG dye molecules. The improved adsorption of dye molecules on the surface of SiO_2, in turn improves the photocatalytic activity of AC-$Bi@SiO_2$ as compared to bare SiO_2.

2. EXPERIMENTAL SECTION

2.1. Materials

Tetraethyl orthosilicate (TEOS, $Si(OC_2H_5)_4$), ethanol (C_2H_5OH), nitric acid (HNO_3), bismuth nitrate pentahydrate ($Bi(NO_3)_3.5H_2O$), activated charcoal, anhydrous ethanol (C_2H_5OH), coumarin and

malachite green ($C_{23}H_{25}ClN_2$) were the guaranteed reagents of Sigma Aldrich and used as supplied. The aqueous solutions were prepared by using double distilled water.

2.2. Synthesis of AC-Bi@SiO_2 nanocomposite sphere

AC-Bi@SiO_2 was synthesized by sol–gel method. The process involves hydrolysis and condensation of metal alkoxides ($Si(OR)_4$) such as TEOS in the presence of HNO_3 [39]. TEOS (10 mL) and C_2H_5OH (20 mL) was mixed together; the resulting mixture was added drop-wise to 20 mL of a 0.1 M HNO_3 (solution A). Then, $Bi(NO_3)_3.5H_2O$ (0.2 M) in a 100 mL beaker (solution B) and sonicated for 30 min. Solution B was added to solution A drop by drop under vigorous stirring at 60 °C for 6 h, then 0.05 M of activated charcoal was added. The mixture was then allowed to stand for 6 h to allow the sol was left to age, dry and shrink. The sol–gel substrate was dried at 100 °C for 1 h in an isotemperature oven. This was followed by further calcination at 500 °C for 2 h. Finally the sol-gel matrix was ground well to obtain AC-Bi@SiO_2 nanocomposite sphere. The obtained composite was found that the 95 wt % of Bi@SiO_2 and 5 wt % of the AC. The bare SiO_2 was synthesized without addition of $Bi(NO_3)_3.5H_2O$ and activated charcoal. Bi-doped SiO_2 was synthesized by the same procedure with $Bi(NO_3)_3.5H_2O$.

2.3. Analysis of hydroxyl radical

The formation of hydroxyl radicals (•OH) are similar to the photocatalytic experiments [40]. PL technique with coumarin as a probe molecule was used to investigate the formation of •OH on the surface of photocatalysts illuminated by UV irradiation.

2.4. Photocatalytic activity

The photocatalytic activity of the AC-Bi@SiO_2 was evaluated by the photodegradation of MG. The light source was a UV lamp. The reaction was maintained at ambient temperature (303 K). In a typical experiment, aqueous suspensions of MG dye (40 mL, 1×10^{-4} M) and 0.1 g of the photocatalysts was placed in a reaction tubes. Prior to irradiation, the suspension was magnetically stirred in the dark to ensure the establishment of an adsorption/desorption equilibrium. The suspension was kept under constant air-equilibrated condition. At the intervals of given irradiation time. The suspension was measured spectrophotometrically (615 nm) by diluting it three times to keep the absorptions within the Beer–Lambert law limit. The photoreaction was also studied by subjecting it to UV-irradiation in the absence of photocatalyst (Nil catalyst) and absence of UV-light with photocatalysts in a reaction (Dark).

2.5. Characterization methods

High-resolution scanning electron microscopy and elementary dispersive X-ray analysis experiments were carried out on a FEI Quanta FEG 200 instrument with EDX analyzer facility at 25 °C. The sample was prepared by placing a small quantity of prepared nanocomposites on a carbon coated copper grid and allowing the solvent to evaporate. High-resolution transmission electron microscopy image was examined using a JEOL 3010 high resolution transmission electron microscope with a UHR polepiece operates at an accelerating voltage of 300 kV. X-ray diffraction spectra was recorded on the X'PERT PRO model X-ray diffractometer from Pan Analytical instruments operated at a voltage of 40 kV and a current of 30 mA with Cu Kα radiation. X-ray photoelectron spectroscopy analysis were performed on a monochromatic Al Kα source instrument (Omicron Nanotechnology, GMBH, Germany) operating at 14 kV and 20 mA for an X-ray power of 280 W. Spectra were collected with a photoelectron

take-off angle of 90° from the sample surface plane with energy steps of 0.10 eV and pass energy of 20 eV. The spectra were referenced to the binding energy of C (1s) (285 eV). The BET method was utilized to calculate the specific surface area of the materials. By using the Barrett–Joyner–Halenda (BJH) model, the pore size distribution was derived from the desorption branches of the isotherms at a relative pressure (P/Po) of 0.98. To determine the textural properties of the synthesized materials, N_2 adsorption–desorption measurements were carried out at 77 K using a Micromeritics ASAP 2020 V3.00 H instrument. Fourier transform-Raman spectra were recorded with an integral microscope Raman system using Bruker RFS27 100 s^{-1} (1064 nm) spectrometer equipped with 1024 X 256 pixels liquefied nitrogen-cooled germanium detector. Measurements were performed using a frequency doubled neodymium doped yttrium aluminium garnet (Nd:YAG). To avoid intensive heating of the sample, the laser power at the sample was not higher than 15 mW. Each spectrum was recorded with an acquisition time of 18 sec. The spectral resolution of this Raman spectrometer was ~2 cm^{-1}. The UV-Visible diffuse reflectance spectra of nanomaterials were recorded with a UV-3600 SHIMADZU (Japan) spectrometer in the range of 800–200 nm. Photoluminescence spectra at room temperature were recorded using a Perkin-Elmer LS 55 fluorescence spectrometer. Nanoparticles were dispersed in chloroform and excited using light of wavelength 300 nm. UV-vis (ultraviolet and visible light) absorbance spectra were measured over a range of 800-200 nm with a Shimadzu UV-1650PC recording spectrometer using a quartz cell with 10 mm of optical path length.

3. RESULTS AND DISCUSSION

3.1. Characterization of the photocatalysts

The HR-SEM images of the Bi@SiO_2 and AC-Bi@SiO_2 are shown in Fig. 1a and 1b. From the HR-SEM images of the nanoparticles possess an almost spherical shape, showing a relatively homogenous distribution of Bi particles throughout the amorphous silica network. Bi@SiO_2 shows an average particle size of 85 nm and AC-Bi@SiO_2 shows an average particle size of 40 nm. The above observation shows that the particle size of Bi@SiO_2 was greater than that of AC-Bi@SiO_2 suggested that in the absence of the supported material. AC acts as a barrier, which controlled the growth of Bi@SiO_2 particles and prevented their aggregation. Additionally, the AC-Bi@SiO_2 agglomerates possess a rough and porous surface, resulting in an increased surface area. Moreover, the increase in the surface area suggests that these nanoparticles could be chemically reactive, therefore suitable for photocatalytic applications [35]. EDX analysis confirms Si, Bi and O are present in Bi@SiO_2 (Fig. 1c), whereas Si, Bi, C and O are present in AC-Bi@SiO_2 (Fig. 1d). EDX analysis clearly displays intense peak at 2.5 keV corresponding to bismuth L1, the Peaks for the elements Si, O and C appearing at 1.7 keV, 0.5 keV and 0.3 keV. Fig. 1e depicts the HR-TEM micrograph of the synthesized AC-Bi@SiO_2. The synthesized composite having well defined spherical shaped with core/shell nanostructure was clearly observed due to the strong contrast between the black cores and gray shells [41], which provides direct evidence that the Bi nanoparticles were encapsulated within the silica shell. The above observation shows that Bi core–SiO_2 shell composite spheres were uniform in size and shape.

The XRD patterns of the SiO_2, Bi@SiO_2 and AC-Bi@SiO_2 nanoparticles are shown in Fig. 2. Fig. 2a shows that bare SiO_2 indicated that no SiO_2 diffraction peaks and broad hump showing that

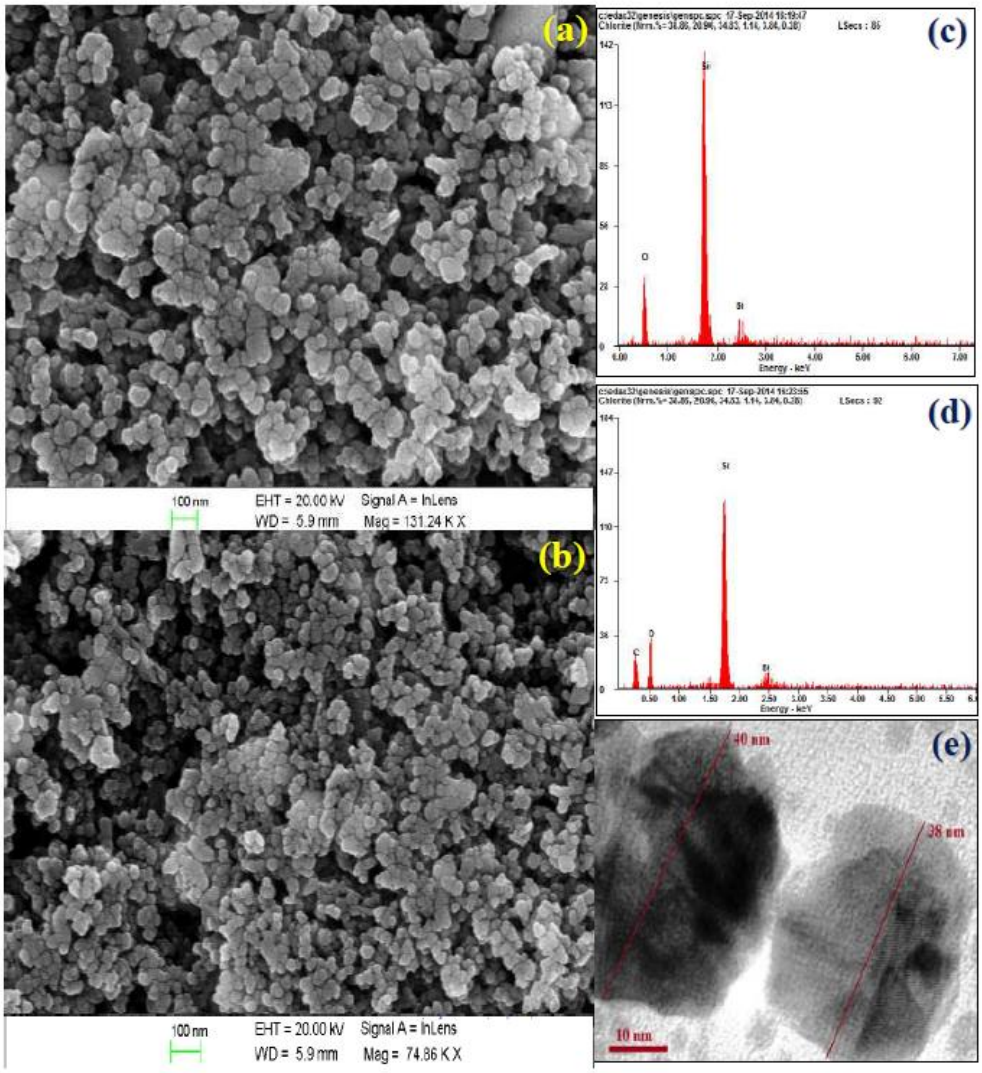

Figure 1. HR-SEM images of (a) Bi@SiO_2 and (b) AC-Bi@SiO_2, EDX analysis of (c) Bi@SiO_2 and (d) AC-Bi@SiO_2 (e) HR-TEM image of AC-Bi@SiO_2 nanocomposite sphere.

the silica was amorphous in nature. The amorphous silica XRD pattern superimposes Bragg reflexes of quartz [29]. Moreover, the appearance of broad peak around at 25° in the top diffraction pattern is assigned to (101) planes in amorphous structure of silica. Bi-doped SiO_2 (Fig. 2b) shows that intense peaks at 22.4°, 25.9°, 40.9°, 46.7° and 55.2° are the diffractions of the Bi (003), Si (101), Bi (110), (113) and Si (103), respectively. It shows Bi was present in the SiO_2 material (JCPDS no. 33-1161 and 85-1330). The obtained XRD (Fig. 2c) of the AC-Bi@SiO_2 shows that intense peaks at 22.3°, 24.3°, 25.6°, 40.8°, 46.5°, 49.9°, 55.5° and 60.7° are the diffractions of the Bi (003), (101), Si (101), Bi (110), (113), C (511), Si (103) and C (161), respectively (JCPDS no. 33-1161, 85-1330 and 50-0927). It has been reported that the encapsulation Bi^{3+} into the silica shells, can be observed from a broad profile appeared around $2\theta=25^{o}$ due to the amorphous silica [42]. The intense peaks at 33.5° and 57.2° are the diffraction of the Bi–SiO_2 crystalline phase corresponds to Bi^{3+} was

doped into the SiO_2 matrix. Furthermore, the XRD peaks corresponding to Bi_2SiO_5 were not found, probably due to the small undetectable amount.

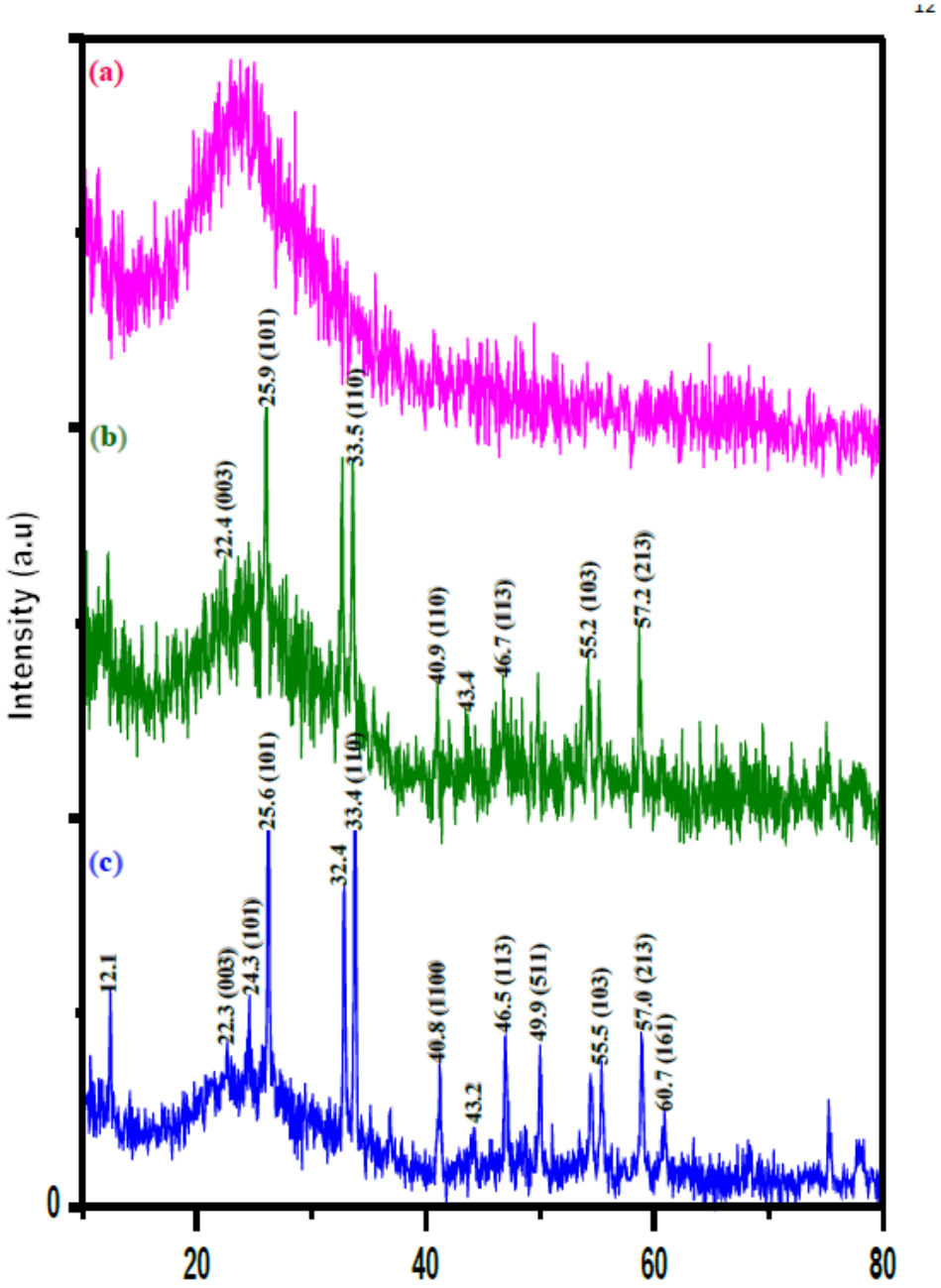

Figure 2. XRD patterns of (a) SiO2, (b) Bi@SiO2 and (C) AC-Bi@SiO2 nanocomposite sphere

The Bi atom into a silica matrix will be in the vibrational state much different from the bare SiO_2. This vibrational energy is sufficient to break the inter-atomic bonds, thus distracting the amorphous silica network and reducing the kinetic barrier to the crystallization [43,44]. It is suggested that the presence of bismuth particles favors crystallization of sol-gel derived silica matrix.

AC has not shown any phase change (Fig. 2c), aggregates may have been formed on crystal borders and on the surface of the Bi@SiO_2. The average crystalline size (*L*) of the SiO_2, Bi@SiO_2 and AC-Bi@SiO_2 particles are calculated by the Debye-Scherrer formula [45], L=0.89λ/βCOSθ where *L* is the crystalline size (in nm), λ is the wavelength (in nm), β is the full width at half maximum intensity (FWHM-in radian), and θ is the Bragg diffraction angle (º). The average crystalline size of SiO_2, Bi@SiO_2 and AC-Bi@SiO_2 was figured out to be about 98.5, 84.5 and 39.5 nm.

XPS was used to determine the presence of elements and to determine their valance states in AC-Bi@SiO_2 nanocomposite sphere. The binding energy peaks of Si, Bi, C and O were analyzed. Survey spectrum in Fig. 3a shows the presence of Si, Bi, C and O. The Si 2p of AC-Bi@TiO_2 is shown in Fig. 3b. Si 2p peak at 108 eV reveal that Silica is in the state of Si^{4+} [46]. In Fig. 3c, the peak of Bi $4f_{5/2}$ is centered at 164 eV reveal that bismuth is in the state of Bi^{3+} [47]. The C 1s peak is attributed to the activated charcoal present in the synthesized nanocomposite sphere (Fig. 3d). The carbon signal (289 eV) in AC-Bi@SiO_2 is likely from the organic precursor used to synthesize of composite sphere. The peak position of the O 1s binding energy is around 537 eV (Fig. 3e) [35]. Comparing with the peak position to those in the Handbook of X-Ray Photoelectron Spectroscopy [48]. The binding energy of the Si 2p peak for pure SiO_2 is 103 eV. The Si 2p peak for AC-Bi@SiO_2 is shifted to 108 eV compared to the Si 2p peak of pure SiO_2. The chemical shift of the Si 2p and the slight shift of O 1s peaks indicated that the Bi^{3+} was encapsulated into a SiO_2 matrix due to Bi-O-Si chemical bonds at the interface of the core-shell. The shift the band gap edge of AC-Bi@SiO_2 to the formation of Bi-O-Si bonds at the core-shell interface and not to a quantum size effect [49].

The corresponding N_2 adsorption–desorption isotherms and BJH desorption pore distribution of the investigated photocatalysts (SiO_2, Bi@SiO_2 and AC-Bi@SiO_2) are shown in Fig. 4. N_2 adsorption–desorption isotherms of representative catalysts are of type IV which is characteristic of mesoporous materials. The H2 hysteresis loop with a steep desorption branch is observed, suggesting the presence of pores with narrow neck, wide-body pores, often referred to as ink-bottle and the pores are formed in the exterior space between the particles [19,50]. Pore size distribution was determined by the BJH model and shows that SiO_2, Bi@SiO_2 and AC-Bi@SiO_2 are given in inset Fig. 4a, 4b and 4c respectively. BET surface area of AC-Bi@SiO_2 (16.4 m^2/g^{-1}) is higher than that of Bi@SiO_2 (13.6 m^2/g^{-1}) and bare SiO_2 (9.1 m^2/g^{-1}). However, the pore volume and pore size of AC-Bi@SiO_2 (0.12 cm^3/g^{-1} and 129 Å) was significantly higher than that of Bi@SiO_2 (0.10 cm^3/g^{-1} and 120 Å) and bare SiO_2 (0.03 cm^3/g^{-1} and 17.7 Å). From these results, it can be concluded that not only enlarged the surface area but also broadened the pore size. The high porosity, higher surface area and larger pore size facilitate the mass transfer of reactants such as oxygen and reaction intermediates [51], which improves photocatalytic activity.

Raman techniques were used to study the structural evolutions of sol-gel silica matrix caused by the presence of metallic particles as a function of the annealing temperatures [44]. Fig. 5 shows the Raman spectra of the Bi@SiO_2 and AC-Bi@SiO_2 calcined at 500 ºC. Silica network bands at 400-490 cm^{-1} and 800 cm^{-1} which have been assigned to the network bending modes and Si-O-Si symmetrical stretching, respectively [52]. The characteristic peaks at 229 cm^{-1} and 374 cm^{-1} attributed to the 2TA; $2E_2$(low) mode, which is one of the characteristic peak of Bi–O bonds [35]. The D1 defect mode at 487 cm^{-1} is assigned to symmetric breathing modes of four-

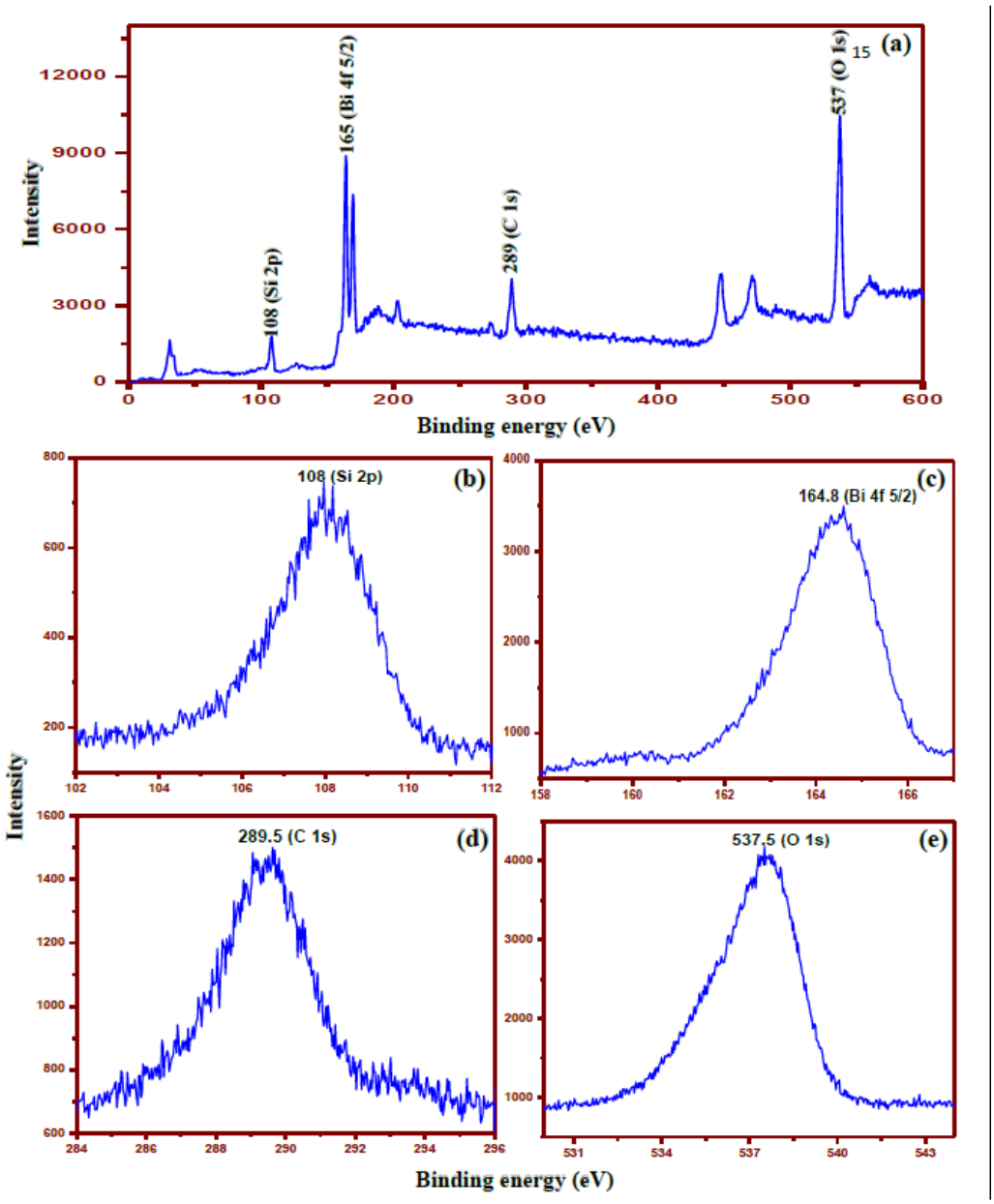

Figure 3. XPS analysis of AC-Bi@SiO_2: (a) survey spectrum, (b) Si 2p, (c) Bi 4f, (d) C 1s and (e) O 1s

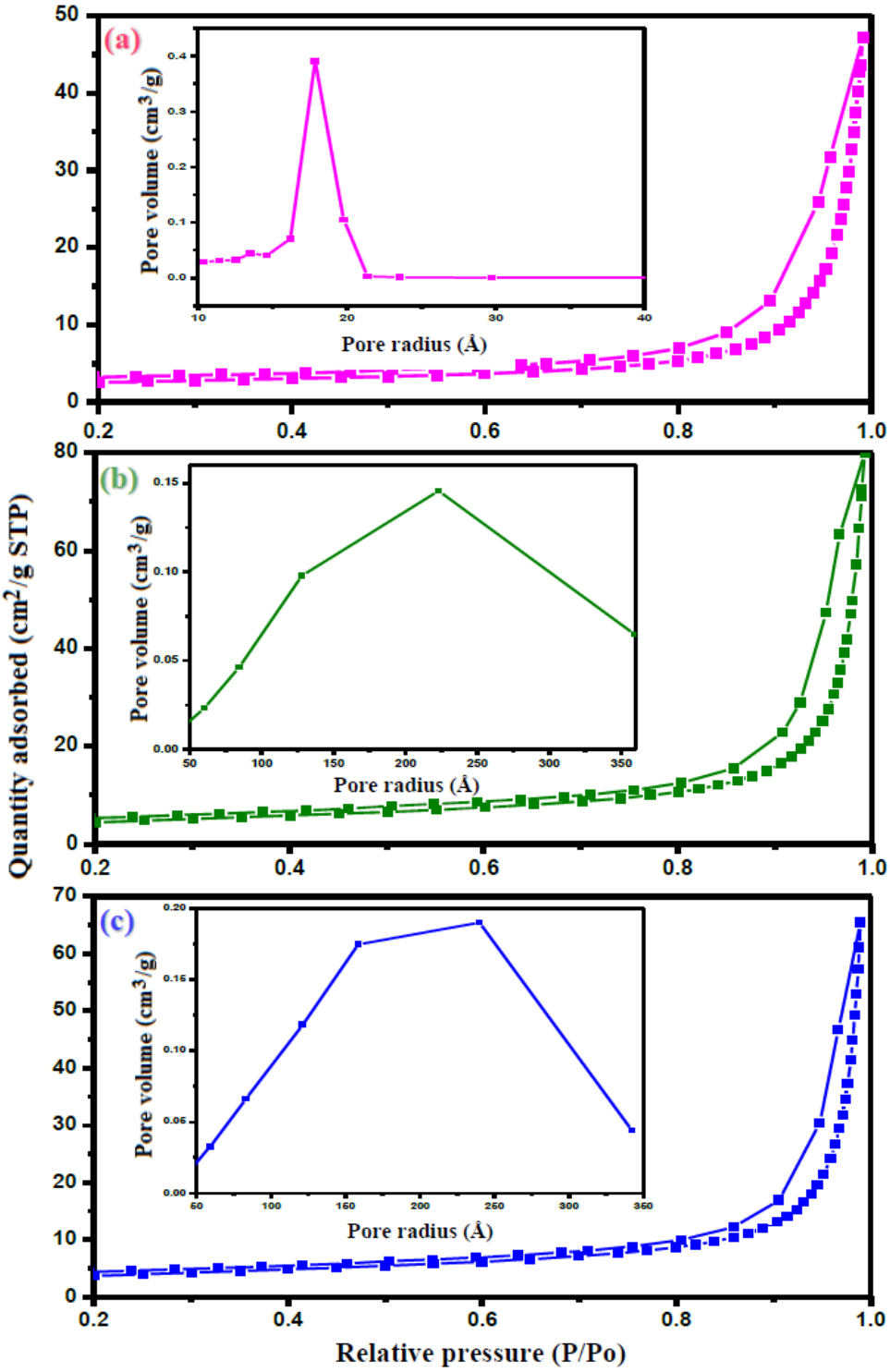

Figure 4. N_2 adsorption–desorption isotherms of (a) SiO_2 (b) $Bi@SiO_2$ and (c) $AC\text{-}Bi@SiO_2$ (Inset: BJH desorption pore distribution)

-membered ring of SiO_2, which is corresponds to Si–O–Si symmetric stretching–bending modes [53]. The characteristic band at 940 cm^{-1} is attributed to the bridging of Bi-O-Si band (Fig. 5a). A_1(LO) peak caused by polar branches appeared at about 546 cm^{-1}, which is the fingerprint for crystalline silicon, increases in intensity with increasing the energy above a certain threshold value. From this observation Bi was present in the silicate matrix. The peak around at 400 cm^{-1} originates from torsional vibrations and O–Si–O bending modes. The vibrational band at 605 cm^{-1} has been assigned to the D2 defect modes attributed to tri-cyclosiloxane ring, respectively. The band around at 800 cm^{-1} corresponds to the motion of silicon against its tetrahedral oxygen cage [44]. Fig. 5b clearly shows that high intensity peak at 1590 cm^{-1} assigned to G-band [54], which corresponds to carbon was present in the AC-Bi@SiO_2 nanocomposite sphere.

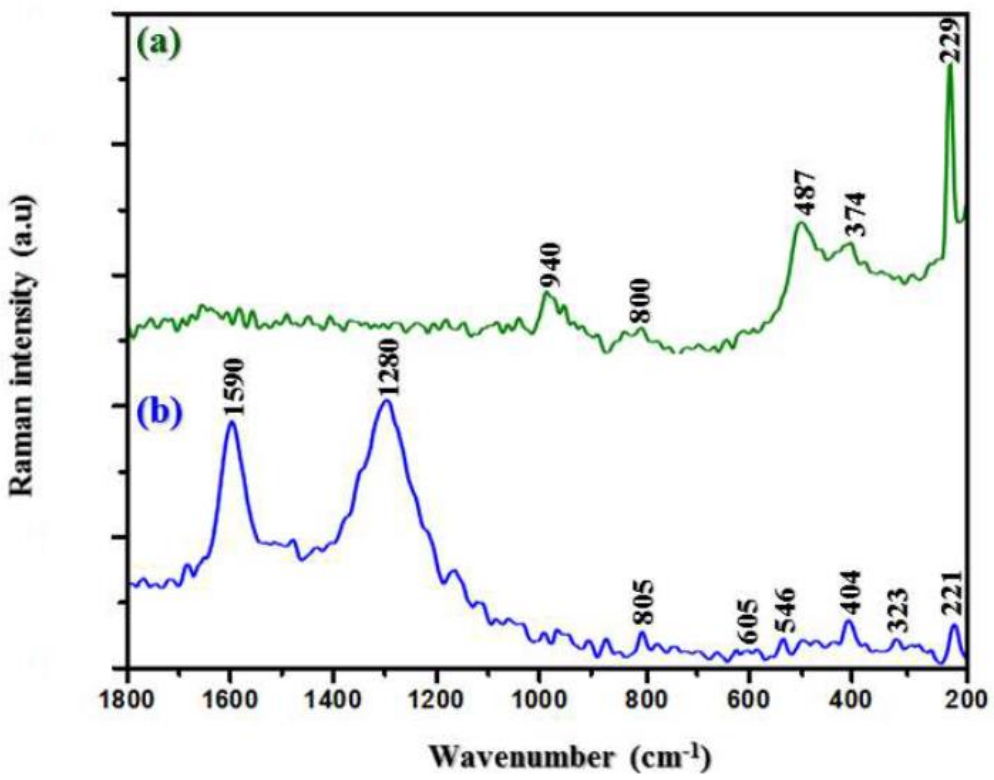

Figure 5. FT-RAMAN spectra of (a) Bi@SiO_2 and (b) AC-Bi@SiO_2

Fig. 6a-c shows the results of UV–vis diffuse reflectance spectra for the synthesized samples. Plots of $[F(R)h\nu]^2$ versus the photon energy (h_V) provide the direct band gap of the synthesized SiO_2, Bi@SiO_2 and AC-Bi@SiO_2 as 3.46, 3.32 and 3.18 eV, respectively. The barrier for electrons at the Si/SiO_2 interface is 3.14 eV, whereas the barrier for holes at the same border is 3.8 eV [55]. The barrier for electrons or holes at the synthesized SiO_2 interface is 3.46 eV. UV–Vis-DRS results demonstrated that the decrease in the direct band gap of AC-Bi@SiO_2 compared to SiO_2 and Bi@SiO_2. These results reveal AC-Bi@SiO_2 will be useful as an effective photocatalyst. In addition, the UV-vis spectrum in the diffuse reflectance mode (R) was transformed to the Kubelka–Munk (KM) function, F(R) values have been

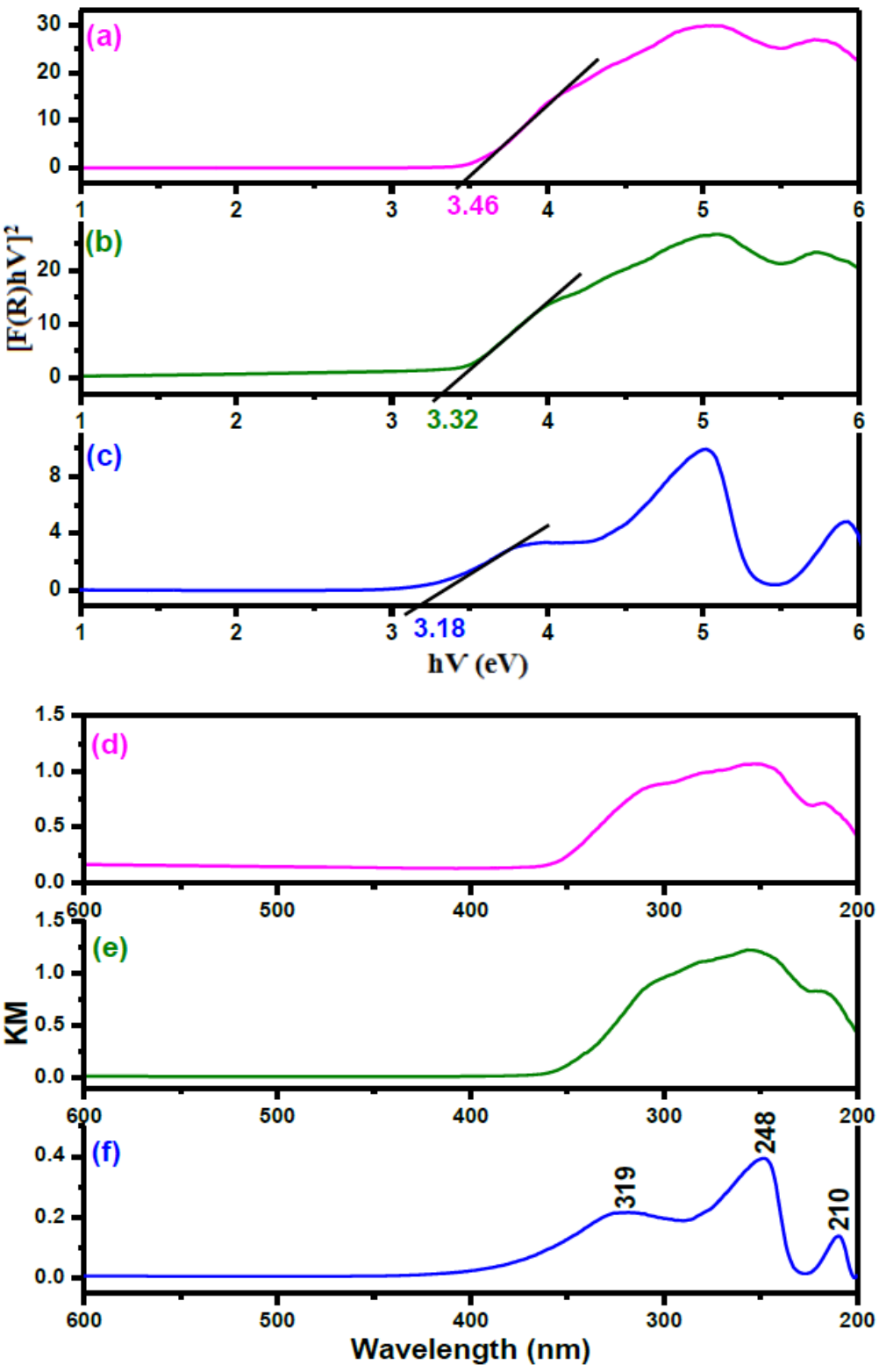

Figure 6. Direct band gap of (a) SiO_2, (b) $Bi@SiO_2$, (c) $AC\text{-}Bi@SiO_2$ and Plot of Kubelka–Munk function versus energy of the light absorbed on the (d) SiO_2, (e) $Bi@SiO_2$, (f) $AC\text{-}Bi@SiO_2$

calculated from the reflectance (R) by application of the Kubelka–Munk algorithm: [F(R) = $(1 - R)^2/2R$] [35]. The KM plot (Fig. 6d-f) shows that all the photocatalysts showed a broad and strong absorption band at around 200–350 nm that has been assigned to the surface defects on silica matrix [23]. As a result, shows a sol-gel silicate matrix would contribute to strong absorption only in the ultraviolet region, which indicates greater photocatalytic activity in the UV region.

The photocatalytic activity of the photocatalysts was essentially determined by the efficiency of the photogenerated electron–hole recombination. Photoluminescence initiates from the recombination of charge carriers; the PL spectra are highly informative to study the recombination of charge carriers [56,57]. Fig. 7a-c shows the PL spectra for the synthesized photocatalysts exhibiting PL emission in the range of 300-500 nm. SiO_2,Bi@SiO_2 and AC-Bi@SiO_2 showed three emissions at 366, 440 and 486 nm. AC-Bi/SiO2 revealed a significant reduction in the intensity, when compared to SiO2 and Bi@SiO2. Which indicates that the AC-Bi@SiO2 possess a lower recombination rate of the photogenerated charge carriers, it also specified that the decrease in trap states on the catalyst surface may slow the recombination process of photogenerated electrons and holes in the AC-Bi@SiO2, which benefit the enhanced photocatalytic activity.

3.2. Hydroxyl radical analysis

In order to confirm the existence of ˙OH on the surface of the photocatalysts illuminated by UV-light was detected by PL technique. The PL emission spectra excited at 350 nm in coumarin solution suspension with SiO_2, Bi@SiO_2 and AC-Bi@SiO_2 were measured at 75 min (Fig. 7d). The characteristic peaks are respectively located at about 387, 438, 487 and 531 nm respectively. The maximum PL intensity was found for AC-Bi/SiO_2 at 75 min, this suggests that the fluorescence is caused by chemical reactions of coumarin with hydroxyl radical [40,58].

Coumarin readily reacts with ˙OH to produce highly fluorescent product, hydroxyl coumarin. This technique has been used in sonochemistry, radiation chemistry and biochemistry for the detection of ˙OH generated in water. This method trusts on the PL signal at 350 nm of the hydroxylation of coumarin with ˙OH generated at the catalyst/water interface. The PL intensity of hydroxyl coumarin is proportional to the amount of ˙OH radicals produced in water. The method is sensitive and specific, needs only a simple standard PL technique. Increase of ˙OH formation on the surface of AC-Bi@SiO_2 can be caused by the better separation of free carriers retarding the recombination reaction in this catalyst, ˙OH produced by an electron and the holes, are the primary oxidative species in a photocatalytic degradation of MG. Moreover, AC-Bi@SiO_2 with enhanced photocatalytic activity produced much more reactive ˙OH was performed.

3.3. Photocatalytic performance of AC-Bi@SiO_2 nanocomposite sphere

The photocatalytic activity of as-synthesized photocatalysts was evaluated by the degradation and decolorization of a typical cationic dye Malachite Green under UV light irradiation. In recent years, UV-based photochemical processes for the removal of hazardous organic compounds have received growing attention because they are efficient, environmentally friendly and cheap. The changes of the UV–Vis spectra during the photodegradation process of the MG dye in the presence of proposed photocatalysts (SiO_2, Bi@SiO_2 and AC-Bi@SiO_2) under UV irradiation are illustrated in Fig. 8a, 8b and 8c. It can be seen from UV–Visible spectra changes, the adsorption peak of MG solution at 615 nm steadily decreased with increasing the irradiation time, and the initial dark green color of the solution gradually turned to light colored. A comparative study of photocatalytic activity of the synthesized catalysts for

photodegradation as well as decolourization of MG was shown in Fig. 8d. AC-Bi@SiO_2 exhibited excellent photocatalytic activity when compared to that of SiO_2 and Bi@SiO_2.

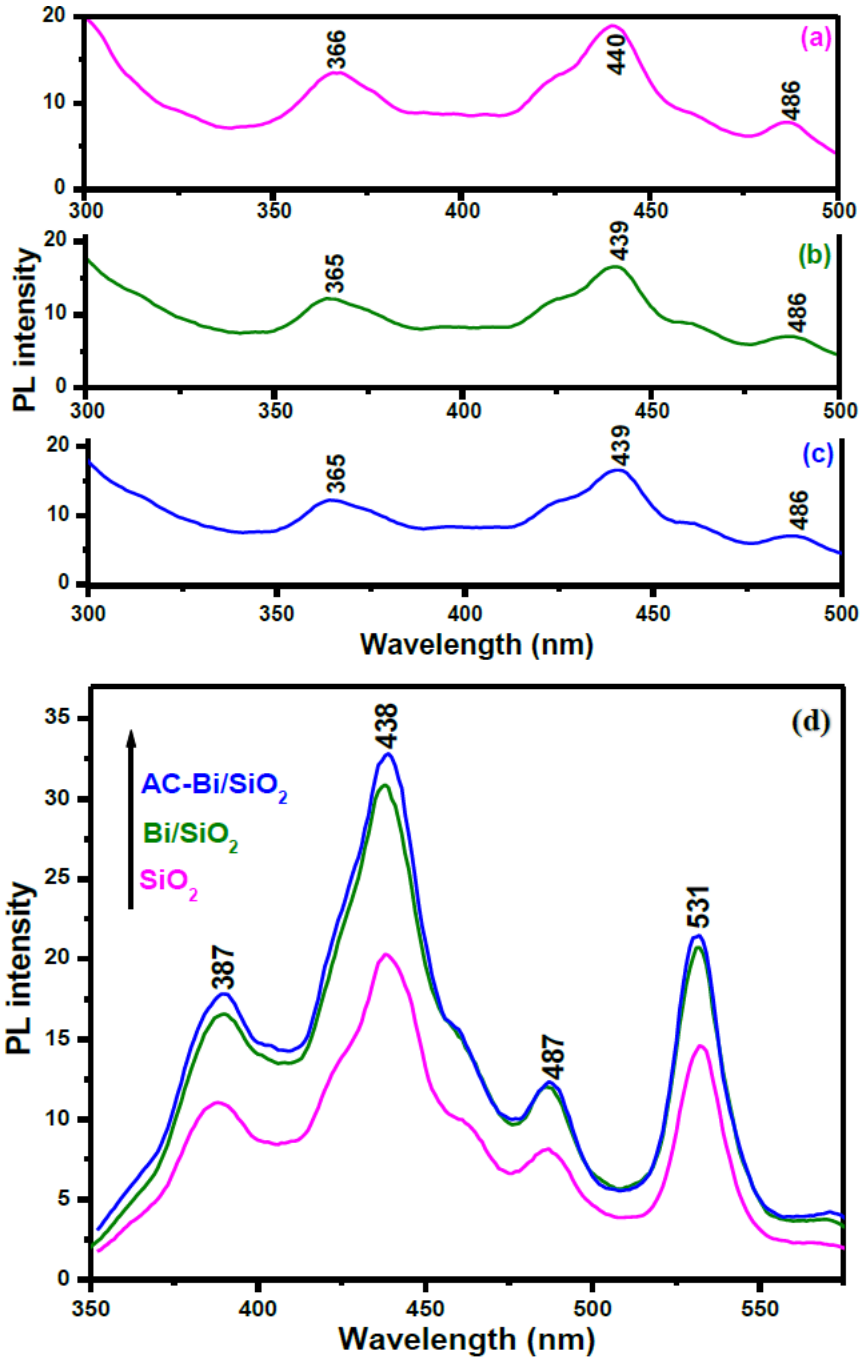

Figure 7. PL spectra of (a) SiO_2, (b) Bi@SiO_2, (c) AC-Bi@SiO_2 and (d) PL spectra of the photocatalysts under excitation at 350 nm in coumarin solution under UV-irradiation at 75 min.

Fig. 9a and 9b shows the time course of percentage degradation and decolourization of MG under UV-light irradiation. After 75 min of irradiation time AC-Bi@SiO_2 can degrade the MG in aqueous solution up to 90% when compared to that of SiO_2 (63%) and Bi@SiO_2 (74%). AC-Bi@SiO_2 can decolorize the MG in aqueous solution up to 95% when compared to that of SiO_2 (70%) and Bi@SiO_2 (79%) respectively. However AC-Bi@SiO_2 exhibited higher photocatalytic activity than SiO_2 and Bi@SiO_2. Under dark conditions, initially there is a decrease in MG concentration with AC-Bi@SiO_2 and this is due to the adsorption of the MG dye on the catalyst surface.

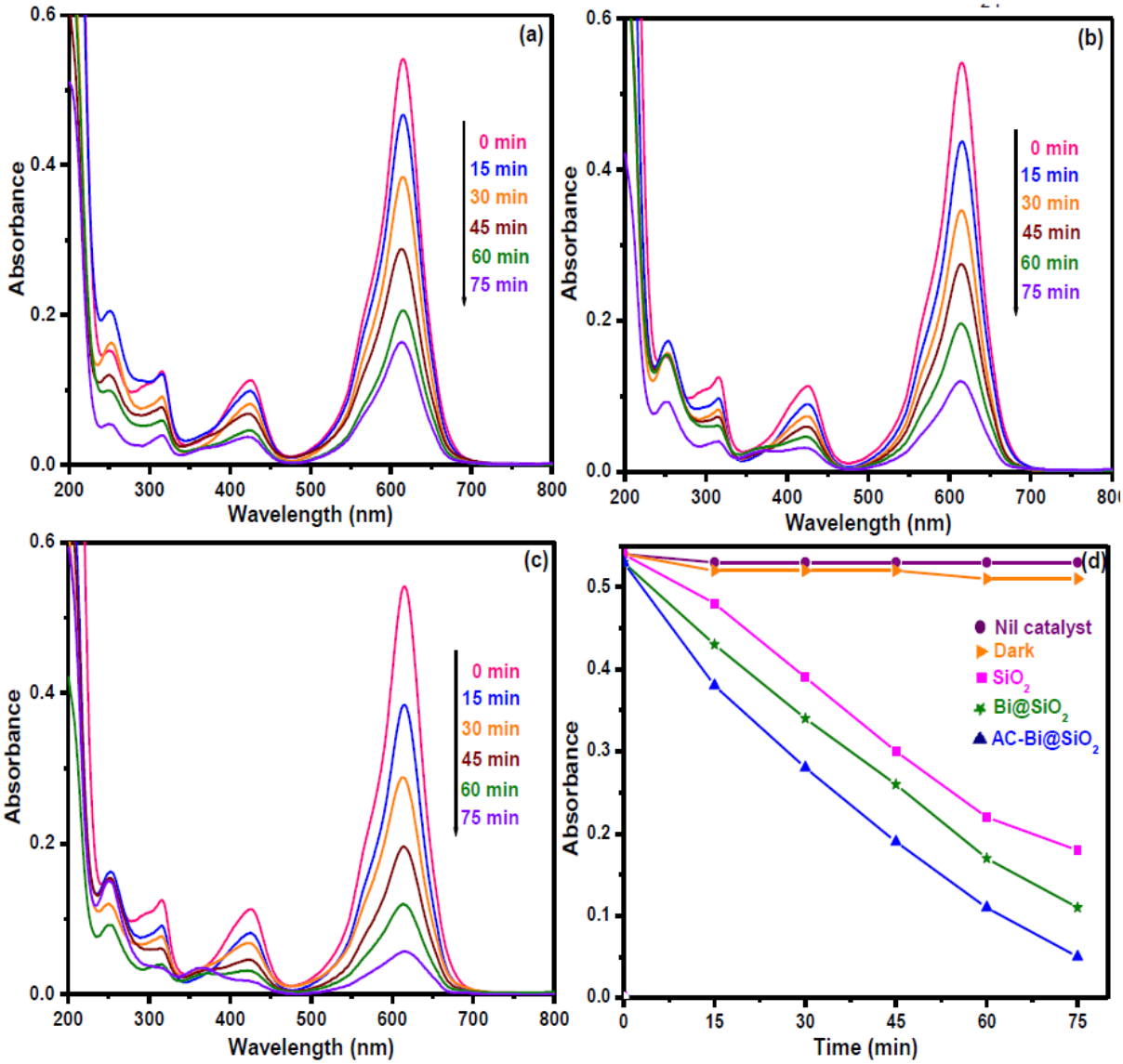

Figure 8. Absorption spectra changes of malachite green solution (1×10^{-4} M, 40 mL) in the presence of photocatalysts (a) SiO_2, (b) Bi@SiO_2 and (c) AC-Bi@SiO_2 under UV-light irradiation at 15 minutes interval. (d) Comparative studies of photocatalytic activity (absorbance vs time (min)) of SiO_2, Bi@SiO_2 and AC-Bi@SiO_2 photocatalysts for photodegradation and decolourization of MG.

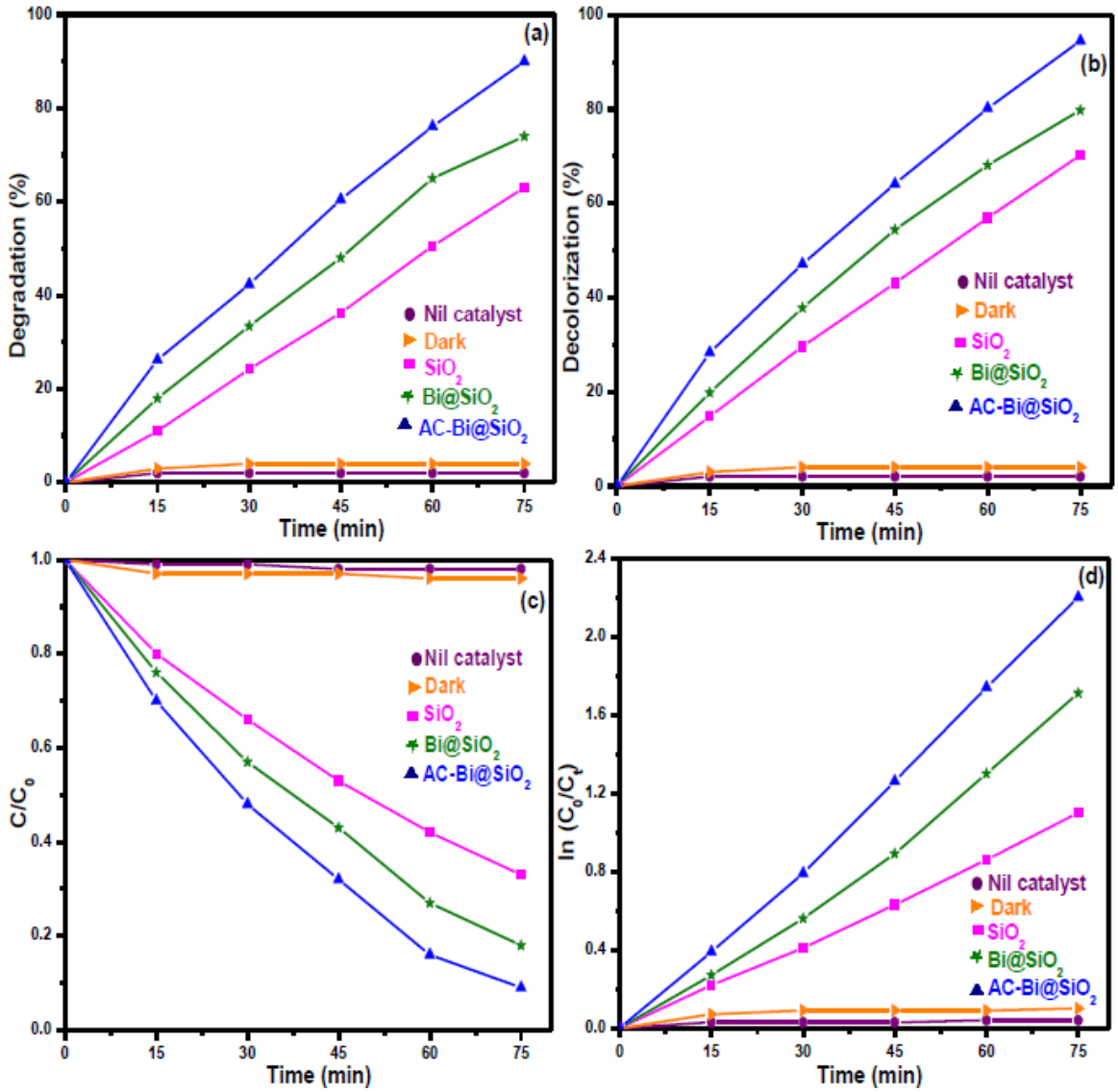

Figure 9. Comparison of photocatalytic activity of SiO_2, $Bi@SiO_2$ and $AC\text{-}Bi@SiO_2$ under UV-light irradiation (a) dye degradation (%) vs 15 min interval, (b) dye decolorization (%) vs. 15 min interval, (c) Kinetic of MG degradation upon irradiation and (d) Photodegraded efficiencies for the SiO_2, $Bi@SiO_2$ and $AC\text{-}Bi@SiO_2$, variations in $\ln(C_0/C_t)$ as function of irradiation time and linear fits of photocatalysts.

Fig. 9c, evaluated by measuring the time dependent degradation efficiency of MG under UV-light irradiation, the photodegradation kinetics of MG on SiO_2, $Bi@SiO_2$ and $AC\text{-}Bi@SiO_2$ were evaluated using the pseudo-first-order model:

$$\ln(C_0/C_t) = K_{app}t \quad (1)$$

Where $K_{app}t$ is the rate constant [min], C_0 is the initial concentration of MG, and Ct is the concentration of MG at reaction time (t) [59], From the results (Fig. 9d), one can see that AC-Bi@SiO_2 showed the highest degradation rate constant, approximately 1.090×10^{-4} sec^{-1}, which was greater than that of SiO_2 (~0.830×10^{-4} sec^{-1}) and Bi@SiO_2 (~0.910×10^{-4} sec^{-1}).

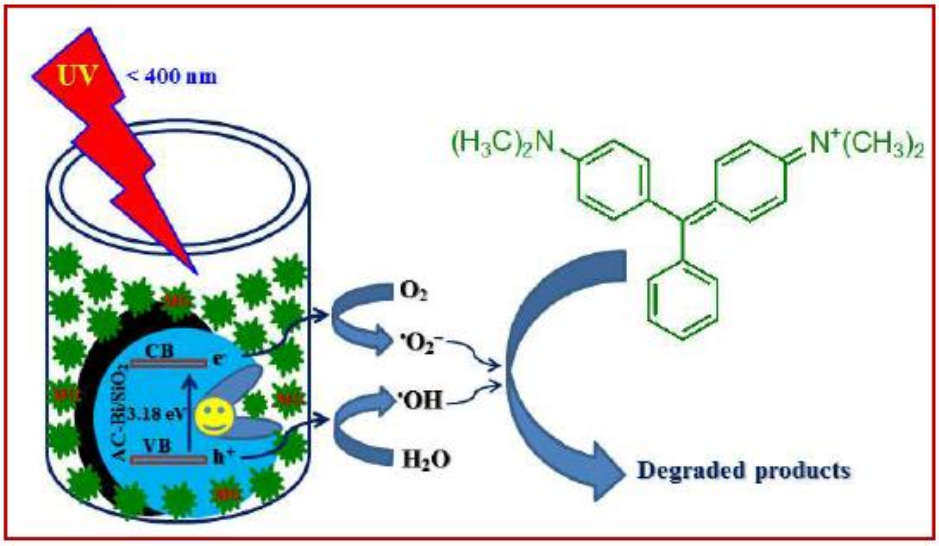

Figure 10. Mechanism of photocatalytic degradation

3.4. Photocatalytic degradation mechanism

When a photon of UV-light strikes the AC-Bi@SiO_2 surface, an electron from its valence band (vb) jumps to the conduction band (cb) leaving behind a positively charged valence band hole (h^+_{vb}). The negative charge is increased in the conduction band electrons (e^-_{cb}) and photocatalytic active centers are formed on the surface of AC-Bi@SiO_2 according to Eqn. 2.

$$\text{AC-Bi@SiO}_2 + h\nu \rightarrow h^+_{vb} + e^-_{cb} \quad (2)$$

The valence band holes react with the chemisorbed H_2O molecules to form $^\bullet OH$ radicals (Eqn. 3). The conduction band electrons (e^-_{cb}) can react with an acceptor, such as dissolved O_2, which consequently is transformed into a super oxide radical anion ($O_2^{\bullet-}$) which leads to the formation of additional $HO_2^\bullet$ in Eqn. 4.

$$(H_2O \rightarrow H^+ + OH^-) + h^+_{vb} \rightarrow H^+ + {}^\bullet OH \quad (3)$$

$$O_2 + e^-_{cb} \rightarrow (O_2^{\bullet-}) + (H^+ + OH^-) \rightarrow HO_2^\bullet + {}^-OH \quad (4)$$

On the other hand, h^+_{vb} could interact with donors, such as ^-OH and $HO_2^\bullet$, to form $^\bullet OH$ radicals (Eqn. 5) [60].

$$HO_2^\bullet + {}^-OH + h^+_{vb} \rightarrow {}^\bullet OH \quad (5)$$

The mechanism of photocatalytic degradation of MG by the surface of SiO_2 doped with Bi^{3+} ion is present during the reaction. Bi^{3+} ions are doped within the SiO_2 matrix and then combine with the conduction band electrons (e^-_{cb}) of SiO_2 to form the corresponding Bi^0 atom, the major role of Bi within the SiO_2 is attributed to the consumption of the electrons and its transmission it to the H^+ ions or O_2. Therefore the retardation of the electron–hole recombination will increase the photocatalytic efficiency of the SiO_2 photocatalyst [61,62] and consequently accelerates hydroxyl radical formation and enhancing the

degradation rate of MG dye initiated by •OH (Eqn. 6), which degrade the dye molecule completely into simpler molecules (Eqn. 7).

$$e^{-}_{cb} + Bi^{3+} \rightarrow Bi^{0} + (H^{+}+O_2) \rightarrow [HO_2^{\bullet} + {}^{-}OH] + h^{+}_{vb} \rightarrow {}^{\bullet}OH \quad (6)$$

$$^{\bullet}OH + MG \rightarrow \text{Degradation products} \quad (7)$$

AC could act as electron carrier and can drive out electrons from Bi@SiO_2 surface and avoid the recombination of photoelectrons (Fig. 10). Thus they often enhanced photocatalytic activity.

4. CONCLUSION

Synthesis of AC-Bi@SiO_2 nanocomposite sphere has been successfully achieved by a simple and cost effective sol-gel method. The presence of Bi^{3+} and AC in the SiO_2 has been revealed by HR-SEM with EDX, HR-TEM, XRD, XPS and FT-RAMAN analysis. Results confirmed the formation of AC-Bi@SiO_2. HR-TEM and XRD analysis of AC-Bi@SiO_2 showed the average particle size of 40 nm. The decrease in the particle size can be related with the observed increase of the surface area. EDX and XRD reveal the presence of Si, Bi, O and C in the AC-Bi@SiO_2. TEM and HR-SEM images showed that the AC-supported on the Bi@SiO_2 core-shell nanocomposite spheres without aggregation. XPS reveals the surface chemical states of elements ($Si^{4+,}$ $Bi^{3+,}$ O 1s and C 1s) in the AC-Bi@SiO_2 and determined the large surface area has been confirmed. UV-vis-DRS demonstrated that the decrease in the direct band gap energy of AC-Bi@SiO_2. Bi^{3+} trap the photo-excited electrons so recombination rate of the electron–hole pair decreases. Increase of the •OH radicals formation during UV irradiation in AC-Bi@SiO_2 was observed due to the better separation of free carriers, however there was no considerable photocatalyst ability to •OH radicals formation on the content of Bi-doped SiO_2 and bare SiO_2. The enhanced photocatalytic activity of AC-Bi@SiO_2 is caused by increasing surface area, decreasing band gap energy, reduction of the recombination of electron-hole pairs and increase of •OH radicals. The former indicates that more photogenerated electrons and holes participate in the photocatalytic reactions, which results in the enhancement of photocatalytic activity. The mechanism of MG degradation is proposed for the higher photocatalytic activity of AC-Bi@SiO_2. This work provides a new pathway to design novel photoactive materials for practical applications in waste water treatment.

ACKNOWLEDGEMENT

S.S. is highly thankful to UGC, New Delhi for granting a major research project. (F. No: 39-771/2010(SR), dt. 06.01.2011)

REFERENCES

[1] Aliyan, H.; Fazaeli, R.; Jalilian, R. Fe_3O_4@mesoporous SBA-15: A magnetically recoverable catalyst for photodegradation of malachite green, *Appl. Surf. Sci.* 2013, *276*, 147– 153.
[2] Rao, K. V. K. Inhibition of DNA synthesis in primary rat hepatocyte cultures by malachite green: a new liver tumor promoter, *Toxicol. Lett.* 1995, *81*, 107–113.
[3] Sayılkan, F.; Asilturk, M.; Tatar, P.; Kiraz, N.; Arpac, E.; Sayılkan, H. Preparation of re-usable photocatalytic filter for degradation of Malachite Green dye under UV and vis-irradiation, *J. Hazard. Mater.* 2007, *148*, 735–744.
[4] Schnick, R. A. The impetus to register new therapeutants for aquaculture, *Prog. Fish Cult.* 1998, *50*, 190–196.
[5] Srivaji, S.; Sinha, R.; Roy, D. Toxicological effects of malachite green, *Aquat. Toxicol.* 2004, *66*, 319–329.
[6] Culp, S. J.; Beland, F. A. Malachite green: a toxicological review, *J. Am. Coll. Toxicol*. 1996, *15*, 219–238.

[7] Nelson, C. R.; Hites, R. A. Aromatic amines in and near the buffalo river, *Environ. Sci. Technol.* 1980, *14*, 147–149.
[8] Chena, C. C.; Lu, C. S.; Chung, Y. C.; Jan, J. L. UV light induced photodegradation of malachite green on TiO_2 nanoparticles, *J. Hazard. Mater.* 2007, *141*, 520–528.
[9] Chang, C. F.; Yang, C. H.; Shu, Y. O.; Chen, T. I.; Shu, M. S.; Liao, I. C. Effects of temperature, salinity and chemical drugs on the in vitro propagation of the Dinoflagellate parasite, Amylodinium ocellatum. *Asian Fish Soc.* 2001, P31.
[10] Schnick, R. A. The Impetus to Register New Therapeutants for Aquaculture, *Prog. Fish Cult.* 1988, *50*, 190-196.
[11] Zhao, J.; Wu, K.; Wu, T.; Hidaka, H.; Serpone, N. Photodegradation of dyes with poor solubility in an aqueous surfactant/TiO_2 dispersion under visible light irradiation, *J. Chem. Soc., Faraday Trans* 1998, *94*, 673–676.
[12] Kominami, H.; Kumamoto, H.; Kera, Y.; Ohtani, B. Photocatalytic decolorization and mineralization of malachite green in an aqueous suspension of titanium(IV) oxide nano-particles under aerated conditions: correlation between some physical properties and their photocatalytic activity, *J. Photochem. Photobiol. A* 2003, *160*, 99–104.
[13] Bessekhouad, Y.; Robert, D.; Weber, J. V. Synthesis of photocatalytic TiO_2 nanoparticles: optimization of the preparation conditions, *J. Photochem. Photobiol*, 2003, *157*, 47–53.
[14] Mohamed, R. M.; Mkhalid, I. A.; Baeissa, E. S.; Al-Rayyani, M. A. Photocatalytic Degradation of Methylene Blue by Fe/ZnO/SiO_2 Nanoparticles under Visible light, J. *Nanotechnol*. 2012, DOI:10.1155/2012/329082.
[15] Bibak, O.; Aliabadi, M. Photocatalytic degradation of malachite green in aqueous solution using TiO_2 nanocatalyst, *J. Bio. & Env. Sci*. 2014, *5*, 301-310.
[16] Zhang, Y. C.; Li, J.; Zhang, M.; Dionysiou, D. D. Size-tunable hydrothermal synthesis of SnS_2 nanocrystals with high performance in visible light-driven photocatalytic reduction of aqueous Cr(VI), *Environ. Sci. Technol*. 2011, *45*, 9324-9331.
[17] Xie, L.; Wang, J.; Hu, Y.; Zhu, S.; Zheng, Z.; Weng, S.; Liu, P. ZrO_2-incorporated $Bi_6O_6(OH)_3(NO_3)_3.1.5H_2O$ with superior photocatalytic activity for degradation of malachite green, *RSC Adv*. 2012, *2*, 9881–9886.
[18] Henry, N.; Evain, M.; Deniard, P.; Jobic, S.; Mentre, O.; Abraham, F. $[Bi_6O_{4.5}(OH)_{3.5}]_2(NO_3)_{11}$: a new anhydrous bismuth basic nitrate. Synthesis and structure determination from twinned crystals, *J. Solid State Chem*. 2003, *176*, 127-136.
[19] Chen, Q.; Shi, H.; Shi, W.; Xu, Y.; Wu, D. Enhanced visible photocatalytic activity of titania–silica photocatalysts: effect of carbon and silver doping, *Catal. Sci. Technol*. 2012, *2*, 1213–1220.
[20] Hoffmann, M. R.; Martin, S. T.; Choi, W.; Bahnemann, D. W. Environmental applications of semiconductor photocatalysis, *Chem. Rev*. 1995, *95*, 69-96.
[21] Kandula, S.; Jeevanandam, P. A facile synthetic approach for SiO_2@Co_3O_4 core–shell nanorattles with enhanced peroxidase-like activity, *RSC Adv*. 2015, *5*, 5295–5306.
[22] Schaefer, C. G.; Vowinkel, S.; Hellmann, G. P.; Herdt, T.; Contiu, C.; Schneider, J. J.; Gallei, M. A polymer based and template-directed approach towards functional multidimensional micro-structured organic/inorganic hybrid materials, *J. Mater. Chem. C* 2014, *2*, 7960–7975.
[23] Yuliati, L.; Tsubota, M.; Satsuma, A.; Itoh, H.; Yoshida, H. Photoactive sites on pure silica materials for nonoxidative direct methane coupling, *J. Catal*. 2006, *238*, 214–220.
[24] Bal, R.; Tope, B. B.; Das, T. K.; Hegde, S. G.; Sivasanker, S. Alkali loaded silica, a solid base: investigation by FTIR spectroscopy of adsorbed CO_2 and its catalytic activity, *J. Catal*. 2001, *204*, 358-363.
[25] Haber, J.; Pamin, K.; Matachowski, L.; Mucha, D. Catalytic Performance of the Dodecatungstophosphoric Acid on Different Supports, *Appl. Catal. A* 2003, *256*, 141-152.

[26] Yoshida H.; Shimizu, T.; Murata, C.; Hattori, T. Highly Dispersed Zinc Oxide Species on Silica as Active Sites for Photoepoxidation of Propene by Molecular Oxygen, *J. Catal.* 2003, *220*, 226-232.
[27] Murata, C.; Yoshida, H.; Kumagai, J.; Hattori, T. Active Sites and Active Oxygen Species for Photocatalytic Epoxidation of Propene by Molecular Oxygen over TiO_2−SiO_2 Binary Oxides, *J. Phys. Chem. B* 2003, *107*, 4364-4373.
[28] Senthilvelan, S.; Chandraboss, V. L.; Karthikeyan, B.; Natanapatham, L.; Murugavelu, M. TiO_2, ZnO and nanobimetallic silica catalyzed Photodegradation of methyl green, *Mater. Sci. Semicond. Process.* 2013, *16*, 185–192.
[29] Chandraboss, V.L.; Senthilvelan, S.; Natanapatham, L.; Murugavelu, M.; Loganathan, B.; Karthikeyan, B. Photocatalytic effect of Ag and Ag/Pt doped silicate non crystalline material on methyl violet - Experimental and theoretical studies, *J. Non-Cryst. Solids* 2013, *368*, 23–28.
[30] Loganathan, B.; Chandraboss, V.L.; Murugavelu, M.; Senthilvelan, S.; Karthikeyan, B. Synthesis and characterization of multimetallic-core and siliceousshell Au/Pt/Ag@SiO_2 sol–gel derived nanocomposites, *J. Sol-Gel Sci. Technol.* 2015, *74*, 1-14.
[31] Da Silva, L. M. L.; Da C. Silva, F.; De Carvalho, A. L.; Marcal, L.; Saltarelli, M.; De Faria, E. H.; Rocha, L. A.; Calefi, P. S.; Ciuffi, K. J.; Nassar, E. J. Influence of the Percentage of TiO_2 Doped into SiO_2 Matrix on Photocatalysis, *ISRN Nanomater*. 2012, DOI:10.5402/2012/304546.
[32] Stober, W.; Fink, A.; Bohm, E. Controlled growth of mono disperse silica spheres in the micron size range, *J. Colloid Interface Sci*. 1968, *26*, 62–69.
[33] Andriantsiferana, C.; Mohamed E. F.; Delmas, H. Photocatalytic degradation of an azo-dye on TiO_2/activated carbon composite material, *Environ. Technol.* 2013, DOI:10.1080/09593330.2013.828094.
[34] Pozzo, R. L.; Baltan, M. A.; Cassano, A. E. Supported titanium oxide as photocatalyst in water decontamination: state of the art. *Catal Today*. 1997, *39*, 219–231.
[35] Chandraboss, V. L.; Kamalakkannan, J.; Prabha, S.; Senthilvelan, S. An efficient removal of methyl violet from aqueous solution by an AC-Bi/ZnO nanocomposite material, *RSC Adv*. 2015, *5*, 25857–25869.
[36] Tsumura, T.; Kojitani, N.; Umemura, H.; Toyoda, M.; Inagaki, M. Composites between photoactive anatase-type TiO_2 and adsorptive carbon. *Appl Surf Sci*. 2002, *196*, 429–436.
[37] Velasco, L. F.; Parra, J. B.; Ania, C. O. Role of activated carbon features on the photocatalytic degradation of phenol, *Appl. Surf. Sci*. 2010, *256*, 5254–5258.
[38] Mezohegyi, G.; van der Zee, F. P.; Font, J.; Fortuny, A.; Fabregat, A. Towards advanced aqueous dye removal processes: A short review on the versatile role of activated carbon, *J. Environ. Manage.* 2012, *102*, 148-164.
[39] Jiang, Z.; Liu, C.; Liu, Y. Formation of silver nanoparticles in an acid-catalyzed silica colloidal solution, *Appl. Surf. Sci*. 2004, *233*, 135-140.
[40] Ishibashi, K. I.; Fujishima, A.; Watanabe, T.; Hashimoto, K. Detection of active oxidative species in TiO_2 photocatalysis using the fluorescence technique, *Electrochem. Commun*. 2000, *2*, 207–210.
[41] Kong, X.; Yu, Q.; Zhang, X.; Du, X.; Gong, H.; Jiang, H. Synthesis and application of surface enhanced Raman scattering (SERS) tags of Ag@SiO_2 core/shell nanoparticles in protein detection, *J. Mater. Chem*. 2012, *22*, 7767–7774.
[42] Yu, M.; Lin, J.; Fang, J. Silica Spheres Coated with YVO_4:Eu^{3+} Layers via Sol−Gel Process: A Simple Method To Obtain Spherical Core−Shell Phosphors, *Chem. Mater*. 2005, *17*, 1783–1791.
[43] Akkopru, B.; Durucan, C. Preparation and microstructure of sol-gel derived silver-doped silica, *J. Sol-Gel Sci. Technol*. 2007, *43*, 227–236.
[44] Pham, D. P.; Huynh, K. K.; Tran, C. V.; Vu, V. Q.; Tran, T. V. V. Preparation and structural characterization of sol-gel-derived silver silica nanocomposite powders, *Int. J. Mater. Sci. Appl.* 2014, *3*, 147-151.
[45] Zhang, Z. H.; Hossain, M. F.; Arakawa, T.; Takahashi, T. Facing-target sputtering deposition of ZnO films with Pt ultra-thin layers for gas-phase photocatalytic application, *J. Hazard. Mater*. 2010, *176*, 973–978.

[46] Kwon, O. S.; Kim, J. H.; Cho, J. K.; Kim, J. H. Triplet−Triplet Annihilation Upconversion in CdS-decorated SiO2 Nanocapsules for sub-bandgap photocatalysis, *ACS Appl. Mater. Interfaces* 2015, *7*, 318−325.
[47] Ma, J.; Chu, J.; Qiang, L.; Xue, J. Synthesis and structural characterization of novel visible photocatalyst Bi–TiO2/SBA-15 and its photocatalytic performance, *RSC Adv*., 2012, *2*, 3753–3758.
[48] Wagner, C. D.; Riggs, W. M.; Davis, L. E.; Moulder, J. F. Handbook of X-ray Photoelectron Spectroscopy; Perkin–Elmer: Eden Prairie, 1979, p. 81.
[49] Lee, H. S.; Koo S. M.; Yoo, J. W. TiO_2-SiO_2 nanoparticles for suppressing photocatalytic activities and improving Hydrophilicity, *J. Ceram. Process. Res*. 2012, *13*, s300-s303.
[50] Sreethawong, T.; Ngamsinlapasathian, S.; Yoshikawa, S. Surfactant-aided sol–gel synthesis of mesoporous-assembled TiO_2–NiO mixed oxide nanocrystals and their photocatalytic azo dye degradation activity. *Chem. Engg. J*. 2012, *192*, 292–300.
[51] Mahyar, A.; Behnajady, M. A.; Modirshahla, N. Characterization and photocatalytic activity of SiO_2-TiO_2 mixed oxide nanoparticles prepared by sol-gel method, *Indian J. Chem*. 2010, *49*, 1593-1600.
[52] Lee, E. L.; Wachs, I. E. In Situ Spectroscopic Investigation of the Molecular and Electronic Structures of SiO2 Supported Surface Metal Oxides, *J. Phys. Chem. C* 2007, *111*, 14410-14425.
[53] Cendrowski, K.; Chen, X.; Zielinska, B.; Kalenczuk, R. J.; Rummeli, M. H.; Buchner, B.; Klingeler, R.; Borowiak-Palen, E. Synthesis, characterization, and photocatalytic properties of core/shell mesoporous silica nanospheres supporting nanocrystalline titania, *J. Nanopart. Res*. 2011, *13*, 5899-5908.
[54] Li, H. H.; Wu, X. L.; Sun, H. Z.; Wang, K.; Fan, C. Y.; Zhang, L. L.; Yang, F. M.; Zhang, J. P. Dual-Porosity SiO_2/C Nanocomposite with Enhanced Lithium Storage Performance, *J. Phys. Chem. C* 2015, *119*, 3495−3501.
[55] Nekrashevich, S. S.; Gritsenko, V. A. Electronic structure of silicon dioxide (A Review), *Phys. Solid State*, 2014, *56*, 207–222.
[56] Sood, S.; Mehta, S. K.; Umar, A.; Kansal, S. K. The visible light-driven photocatalytic degradation of Alizarin red S using Bi-doped TiO_2 nanoparticles, *New J. Chem*. 2014, *38*, 3127–3136.
[57] Subash, B.; Krishnakumar, B.; Swaminathan, M.; Shanthi, M. Highly efficient, solar active and reusable photocatalyst, Zr loaded Ag-ZnO for Reactive Red 120 dye degradation with synergistic effect and dye sensitized mechanism, *Langmuir*, 2013, *29*, 939−949.
[58] Yu, T.; Tan, X.; Zhao, L.; Yin, Y. X.; Chen, P.; Wei, J. Characterization, activity and kinetics of a visible light driven photocatalyst: cerium and nitrogen co-doped TiO_2 nanoparticles, *Chem. Eng. J*., 2010, *157*, 86–92.
[59] Zhang, S.; Li, J.; Zeng, M.; Li, J.; Xu, J.; Wang, X. Bandgap Engineering and Mechanism Study of Nonmetal and Metal Ion Codoped Carbon Nitride: C+Fe as an Example, *Chem. Eur. J*. 2014, *20*, 9805–9812.
[60] Fu, G.; Cai, W.; Gan, Y.; Jia, J. An ambience-induced optical absorption peak for Au/SiO_2 mesoporous assembly. *Chem. Phys. Lett*. 2004, *385*, 15–19.
[61] Sakthivel, S.; Shankar, M. V.; Palanichamy, M. Enhancement of photocatalytic activity by metal deposition: characterisation and photonic efficiency of Pt, Au and Pd deposited on TiO_2 catalyst, *Water Res*. 2004, *38*, 3001–3008.
[62] Mahmoud, M. A.; Poncheri, A.; Badrc, Y.; Abd El Wahed, M. G. Photocatalytic degradation of methyl red dye, *S. Afr. J. Sci.* 2009, *105*, 299–303.

The authors declare no conflict of interest

© 2015 By the Authors; Licensee Borderless Science Publishing, Canada. This is an open access article distributed under the terms and conditions of the Creative Commons Attribution license http://creativecommons.org/licenses/by/3.0